Design of magnetic polar double-double perovskite oxides through cation ordering

Monirul Shaikh,[1,*] Duo Wang [2], and Saurabh Ghosh [1,†]

[1]*Department of Physics and Nanotechnology, SRM Institute of Science and Technology, Kattankulathur 603 203, Chennai, India*
[2]*Faculty of Applied Sciences, Macao Polytechnic University, Macao SAR 999078, China*

Starting from the centrosymmetric MnRMnSbO$_6$ compound, we explore the realm of magnetic polar double-double perovskite oxides characterized by significant ferroelectric polarization. Employing symmetry operations, first-principles methodologies, and Monte Carlo simulations, our investigation delves into the structural, magnetic, ferroelectric, and electronic attributes of the polar LaFeMnNiO$_6$ and LaTiMnNiO$_6$ compounds. Structural analysis uncovers that the paraelectric-ferroelectric phase transition is intricately linked to the Fe/Ti displacement of square-planar Fe/TiO$_4$. Notably, the magnetic LaFeMnNiO$_6$ and LaTiMnNiO$_6$ compounds demonstrate robust ferroelectric polarizations, measuring 20.0 and 21.8 μC/cm^2, respectively, accompanied by minimalist forbidden energy gaps of 1.40 and 1.18 eV using the generalized gradient approximation $+ U$ method. Furthermore, we pinpoint elevated magnetic transition temperatures for these compounds. Additionally, our study scrutinizes the energies associated with diverse spin configurations and identifies potential minimum decomposition pathways into stable oxides. This comprehensive analysis ensures the meticulous formation of the LaFeMnNiO$_6$ and LaTiMnNiO$_6$ compounds.

I. INTRODUCTION

Double perovskite oxides (DPOs) with the common chemical formula A_2BB'O$_6$ have been the subject of intense research due to their implications for sciences and modern-day technologies. They exhibit important physical properties, including ferroelectricity, ferro- and ferrimagnetism, and so on [1–5]. In the DPO family a framework of corner-shared BO$_6$ octahedra forms a three-dimensional network, and large A-site cations are accommodated at the 12-coordinated cuboctahedral cavities [6]. In addition, the A and B sublattices can be ordered in various ways, such as in layers, columns, and in rocksalts. There are a good number of perovskite oxides that reportedly show large ferroelectric distortions with high polarization values but with negligible magnetization values [7,8].

Combining cation orderings with chemical substitution in the perovskite oxide family is worth exploring for multiferroic properties where ferroelectricity and magnetism can coexist [9–11]. $AA'BB'$O$_6$ DPOs, where A and A' are alkaline-earth and rare-earth ions and B and B' are transition metal ions, have been predicted and extensively studied for multiferroic properties where ferroelectricity and magnetism can coexist [9–13]. Due to the structural and compositional flexibility of $AA'BB'$O$_6$ DPOs, both A and B sublattices can host a large number of atomic combinations. Recently, we realized the importance of cation ordering in both A and B sublattices to design polar magnetic metals and insulators in the DPO family [14]. Leveraging machine learning, we have pinpointed key

features that contribute to stabilizing the system, leading to A-site layered B-site rocksalt ordering [15]. Additionally, our investigation has revealed that the emergence of ferroelectricity is attributed to an incommensurate cation radius mismatch between successive AO and $A'O$ layers (within A-site layered ordering) and structural distortion responsible for ferroelectric switching in DPOs [16].

Double-double perovskite oxides (DDPOs) are characterized by the same formula as DPOs, i.e., $AA'BB'$O$_6$, but now, three-cation sites are occupied by transition metals (TMs), representing a potential class of materials in which functional properties, including multiferroicity, can be explored [17–21]. A unique feature of these perovskite oxides is that the different atomic sites, i.e., A', B, and B', can accommodate magnetic transition metals with the possibility of enhanced magnetic interactions [18,21]. However, the first reported DDPO was CaFeTi$_2$O$_6$, which has only one magnetic (Fe) site [22]. It crystallizes in the tetragonal centrosymmetric space group $P4_2/nmc$ with 10-fold Ca coordination, tetrahedral Fe coordination, and another square-planer Fe coordination. In recent years, the A-site ordered DDPO CaMnTi$_2$O$_6$ with coordination similar to CaFeTi$_2$O$_6$ at the A sublattices has attracted attention owing to its ferroelectric distortion with a large band gap ~ 3.0 eV [17,19,20]. A set of similar DDPOs, MnRMnSbO$_6$ ($R =$ La, Pr, Nd, Sm) with both A-site and B-site cation ordered phases, has been synthesized [18]. These DDPOs show large magnetization, but they crystallize in the tetragonal centrosymmetric space group $P4_2/n$ with no ferroelectric polarization [18,21].

In addition to the cation orderings at the A and B sublattices, 15 different tilting patterns lower the symmetry from cubic $Pm\bar{3}m$ and give rise to various fascinating physical properties [6]. From these patterns, a few Glazer patterns,

*msk.phe@gmail.com
†saurabhghosh2802@gmail.com

such as $a^+a^+a^+$, $a^0b^+b^+$, $a^0b^+b^-$, and $a^-a^-c^+$, have been explored for A-site cation ordered DPOs with in-phase $(+)$, out-of-phase $(-)$, and no (0) rotations of the BO_6 octahedra [23,24]. The $a^+a^+c^-$ rotational pattern [19,25] with A/A' cation ordered DDPOs can lead to ferroelectric distortion into the structure. Thus, the B-site rocksalt A-site columnar double-double perovskite oxides with appropriate rotational patterns hold promise for fabricating magnetic materials with substantial ferroelectric polarization.

In this work, our focus is on the deliberate design of magnetic ferroelectrics. We aim to achieve this by introducing $a^+a^+c^-$ octahedral rotations within MnRMnSbO$_6$ DDPOs. This design strategy involves cation ordering at both A and B sublattices, coupled with chemical substitution. Within the first-principles framework, we discuss the origin of ferroelectricity, band gap opening, and high magnetic transition temperatures in the polar LaFeMnNiO$_6$ (LFMNO) and LaTiMnNiO$_6$ (LTMNO) compounds. We study the stability of these compounds for different spin configurations and possible minimum decomposition pathways into the stable oxides.

II. COMPUTATIONAL METHODS

Density functional theory (DFT) [26] calculations are performed for the optimization of geometry, total energy, and polarization using the Berry phase method [27] as implemented in the Vienna *Ab initio* Simulation Package (VASP) [28]. The k integration in the Brillouin zone is incorporated using Γ-centered $4 \times 4 \times 4$ points for geometry optimization and $8 \times 8 \times 8$ points for self-consistent calculations using a 520.0 eV energy cutoff. We considered the generalized gradient approximation augmented by the Hubbard U corrections (GGA+U) [29] to describe the exchange-correlation effect. To consider d-d Coulomb interactions, we employ U_E [29] ($= U - J_H$, where J_H is Hund's exchange parameter) of 0.0 eV for Ti d [19], 4.0 eV for both Mn d and Fe d, and 6.0 eV for Ni d [14] electrons. The exchange-correlation part is estimated by the Perdew-Burke-Ernzerhof revision for solids (PBEsol) functional [30]. The total energy and Hellmann-Feynman force are carefully converged for individual atoms down to 1 μeV and 1 meV/Å, respectively. To draw and analyze the geometry of our three-dimensional systems, we implement the Visualization for Electronic and Structural Analysis (VESTA) software [31]. We perform phonon calculations on the fully relaxed $a^+a^+c^-$ rotated LaMMnNiO$_6$ DDPOs (where $M =$ transition metal) to find polar structural distortion using the finite-difference method as implemented in VASP [32]. The symmetry operations are performed with the help of the ISODISTORT tool [33].

Next, we utilize the optimized structure as input for the calculations of interatomic exchange parameters by means of the magnetic force theorem [34] using the full-potential linear muffin-tin orbital in the RSPT code [35]. Last, an effective spin Hamiltonian is constructed, and phase transition temperatures are obtained by conducting classical Monte Carlo simulations, as implemented in the UPPASD package [36]. Exchange parameters are calculated using the full-potential linear muffin-tin orbital code RSPT [35], and these parameters are then used as input for classical Monte Carlo simulations, as implemented in the UPPASD package [36]. Supercells consisting of
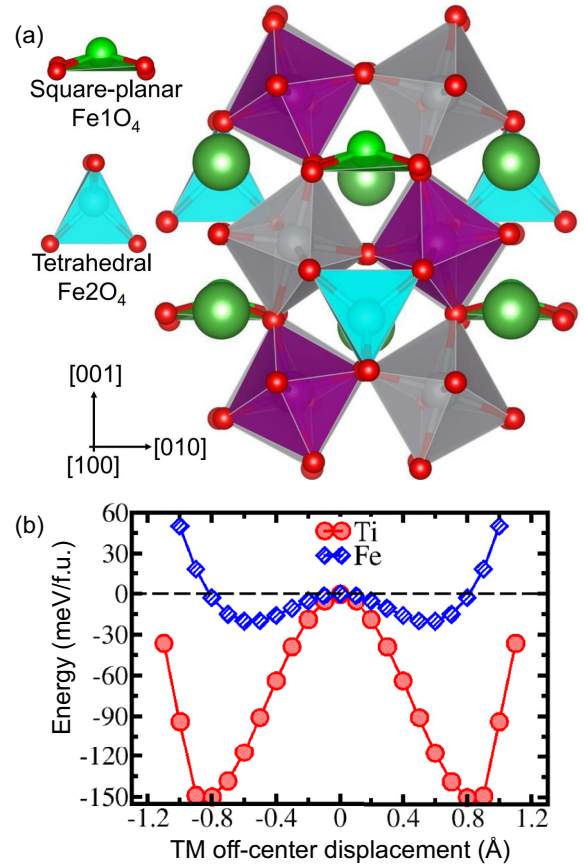

FIG. 1. (a) Crystal structure of ferroelectric LaFeMnNiO$_6$ DDPO. B-site NiO$_6$ and MnO$_6$ octahedra are arranged in a rocksalt-type order, whereas A-site La and Fe are ordered in columns parallel to the crystallographic c direction. Further, Fe A sites govern Fe1O$_4$ and Fe2O$_4$ with square-planar and tetrahedral environments, respectively. The La, Mn, Ni, and O atoms are described by green, magenta, silver, and red balls, respectively. (b) The double-well potential of LFMNO (blue rhombuses) and LTMNO (red circles) as a function of Fe/Ti off-center displacements from the square-planar environment shown in Fig. 1(a).

approximately 60000 magnetic atoms are adopted as the structural model. An annealing process is simulated by performing calculations that start at high temperatures and are gradually decreased to 0 K. To ensure that the magnetic properties obtained at each temperature are in their equilibrium state, an initial simulation of 50000 steps is performed.

We calculate the formation energies for each DDPO proposed in this work by considering the decomposition reaction of the DDPOs via the most probable reaction pathways. Many possible reaction sequences can produce these DDPOs, and

TABLE I. Intriguing physical properties of LFMNO and LTMNO DDPOs.

Systems	Space group	Band gap E_g (eV)	Polarization (μC/cm^2)	Magnetization (in units of μ_B/f.u.)	T_C (K)
LFMNO	$P4_2$	1.40	20.0	5.0	225
LTMNO	$P4_2$	1.18	21.8	0.0	48

TABLE II. Crystal structure information for LaMMnNiO$_6$, with M = Fe and Ti.

System	Lattice parameters (Å)			Cell volume (Å^3)
	a	b	c	
LFMNO	7.55	7.55	7.74	441.20
LTMNO	7.65	7.65	7.76	454.44

each of them could lead us to different formation energies, which could give erroneous results. Hence, to find the correct formation energy, we find the minimum energy reaction sequence to produce these DDPOs.

III. RESULTS AND DISCUSSION

A. Structural and ferroelectric properties

In our pursuit of notable magnetic polar materials, specifically LFMNO and LTMNO, we undertake an exploration of a series of DDPOs based on $3d$ transition metals. These materials feature A' sites, representing Ti, V, Cr, Mn, Fe, Co, Ni, and Cu in LaA'MnNiO$_6$-type perovskites. The crystal structure of the A-site ordered DDPO is illustrated in Fig. 1(a), adopting tetragonal polar (noncentrosymmetric) $P4_2$ symmetry and displaying substantial ferroelectric polarization (see Table I). A detailed structural and symmetry analysis reveals that the polar $P4_2$ space group follows an $a^+a^+c^-$ (Fe/Ti)O$_6$ octahedral rotation pattern akin to the $P4_2/nmc$ structure observed in the synthesized CaFeTi$_2$O$_6$ DDPO [22]. Recently, Ji *et al.* suggested that A-site columnar and B-site rocksalt-ordered DDPOs result in the centrosymmetric $P4_2/n$ space group [21]. However, in contrast to their findings, we present A-site columnar and B-site rocksalt-ordered DDPOs exhibiting a polar $P4_2$ structure. Notably, our design accommodates magnetic TMs on both the B and B' sublattices in addition to a TM at the A' site, adding a layer of versatility to the system.

The La cations acquire a 10-coordinated geometry, while both Mn and Ni at the B sites form BO$_6$ octahedra almost equally tilted along the crystallographic c axis. The TMs, on the other hand, at the A' site show two nonequivalent geometries in columns, i.e., (Fe/Ti)O$_4$ tetrahedral (TH) and (Fe/Ti)O$_4$ square planar (SP), as shown in cyan and green, respectively, in Fig. 1(a). Further, the space group $P4_2$ allows both Fe^{3+} (d^5) and Ti^{4+} (d^0) at the SP site to move along the crystallographic c direction, leading to breaking of an inversion center, similar to what happens in Refs. [17,19]. The absence of a center of symmetry steers ferroelectricity into the systems. Detailed information on the crystal structures,

magnetic moments, and charge states of these compounds is provided in Tables II–IV. Nonetheless, total energy as a function of polar distortion for Ti^{4+} (d^0) in LaTiMnNiO$_6$ is comparable to that of PbTiO$_3$ [37]. However, Fe^{3+} (d^5) in LaFeMnNiO$_6$ exhibits a pronounced depth of the double well compared to CaMnTi$_2$O$_6$, as shown in Fig. 1(b) [19].

We next examine the group-subgroup relation that connects the $P4_2$ (No. 77) phase with the reference $P4_2/mmc$ (No. 131) high-symmetry structure (without any distortions) by implementing ISODISTORT [38]. The decomposition of the $P4_2$ phase with reference to $P4_2/mmc$ symmetry provides us with three contributing structural distortions. These are out-of-phase rotated $a^0a^0c^-$ (Fe/Ti)O$_6$ octahedra with the irreducible representation (irrep) Γ_3^+, in-phase $a^+a^+c^0$ rotation of (Fe/Ti)O$_6$ octahedra with irrep M_4^-, and off-centering of the (Fe/Ti) cation of SP (Fe/Ti)O$_4$ from the center of symmetry with irrep Γ_3^-, as shown in Figs. 2(a)–2(c). The normalized mode amplitudes are 0.34 (0.36), 0.50 (0.53), and 0.16 (0.11) Å for Γ_3^+, M_4^-, and Γ_3^-, respectively, for LTMNO (LFMNO). In Fig. 1(b) we plot the double wells for the ferroelectric Γ_3^- mode for both compounds. The normalized mode amplitude of the Γ_3^- mode is 0.11 and 0.16 Å for LFMNO and LTMNO, respectively. Although there is a complex interplay between all three modes, from the double-well depths it is clear that Ti^{4+} ($3d^0$) is more pronounced than Fe^{3+} ($3d^5$). Moreover, the symmetry operation indicates the phase transition chain described in Fig. 2(d). Coupling between in-phase $a^+a^+c^0(M_4^-)$ and out-of-phase $a^0a^0c^-(\Gamma_3^+)$ octahedra reduces the symmetry to the centrosymmetric $P4_2/n$ (No. 86) phase. It is worth mentioning that to realize the bilinear coupling between the in-phase rotation ($a^+a^+c^0$) and out-of-phase rotation ($a^0a^0c^-$) of TiO$_6$ octahedra we undertake an extensive study. We start with a perturbed $a^0a^0c^0$ high-symmetry structure and perform complete relaxation. Once the relaxation is done, we decompose all the intermediate structures obtained through ionic iterations with reference to the ideal high-symmetry structure. The corresponding energies from ionic iterations are noted with respect to the ideal high-symmetry structure in Table S1 of the Supplemental Material [39]. Then, to find the coupling nature between in-phase rotation ($a^+a^+c^0$) and out-of-phase rotation ($a^0a^0c^-$) of TiO$_6$ octahedra we pursue several trial Landau models of the phase transition. Our effort shows that the following Landau model of the phase transition fits the best:

$$F = F_0 + a_1 Q_{\Gamma_3^+}^2 + a_2 Q_{M_4^-}^2 + \alpha Q_{\Gamma_3^+} Q_{M_4^-}. \quad (1)$$

The constant F_0 term is set to unity. a_1 and a_2 are two arbitrary constants. The coupling coefficient α between in-phase rotated M_4^- and out-of-phase rotated Γ_3^+ distortions is found to be -1.75 (arbitrary units). This negative sign implies the

TABLE III. Magnetic moments and charge states of LaMMnNiO$_6$ DDPOs.

System	Magnetic moment μ_B			Total magnetic moment (in units of μ_B/f.u.)	Charge state		
	A' site	B site	B' site		A' site	B site	B' site
LFMNO	4.21	3.16	1.71	5.00	3+	4+	2+
LTMNO	0.00	3.82	1.74	0.00	4+	3+	2+

TABLE IV. Bond angles and bond lengths of LaMMnNiO$_6$ DDPOs.

System	Average bond angle (deg)		Average bond length (Å)			
	O-M_{SP}-O	Mn-O-Ni	SP M-O	TH M-O	Mn-O	Ni-O
LFMNO	86.8	141.7	2.02	1.94	1.96	2.03
LTMNO	84.0	139.9	1.98	1.87	2.02	2.04

energy gain is due to the coupling between these two structural distortions. Further reduction in symmetry to polar $P4_2$ occurs by inserting the Γ_3^- mode into the $P4_2/n$ phase.

B. Polar magnetic behaviors from electronic structure calculations

Next, we investigate the stability of the working compounds in various spin configurations. In the case of the $La^{3+}Fe^{3+}Mn^{4+}Ni^{2+}O_6$ DDPO, the A'-site Fe atoms are adapted within the cavity of (Mn/Ni)O$_6$ octahedra. Therein, the nearest-neighbor distances decrease significantly. Consequently, the structure exhibits a complex magnetism within the collinear spin configuration. To achieve a proper magnetic ground state in the collinear spin configuration for LFMNO system, we consider all possible spin configurations between Fe^{3+}, Mn^{4+}, and Ni^{2+}, which are described in Fig. 3. From these spin configurations, a complex ferrimagnetic configuration is found to be the magnetic ground state, as shown in Fig. 4(a). The corresponding electronic structure is shown in Fig. 4(b). Other collinear spin configurations are found to be stable within an energy window of $\sim$120 meV/f.u. A set of similar complex ferrimagnetic compounds was synthesized previously, but all of them were found to be in the centrosymmetric $P4_2/n$ space group [40]. All the nearest-neighbor Fe spins are aligned in opposite directions, leading to a net-zero moment from the Fe site in the system. Thus, Fe-Fe interactions are antiferromagnetic. A weak antiferromagnetic (AFM) Fe^{3+}-O-O-Fe^{3+} superexchange interaction is found in the Fe^{3+} layers. The

Fe^{3+} (d^5) displacement from the square-planar environment with a non-d^0 configuration leads to the breaking of an inversion center, similar to what occurs in Ref. [20]. Further, Fe spins interact antiferromagnetically with both Mn and Ni spins. Consequently, ferromagnetic (FM) interactions are found between Mn and Ni spins. These FM interactions govern a net $5.00\mu_B$/f.u. magnetization in the system (Table I). Since the nearest-neighbor distances decrease, we can expect even stronger magnetic exchange interactions compared to $CaMnTi_2O_6$. The magnitudes of the Fe moments ($4.21\mu_B$/Fe) of SP and TH FeO$_4$ are found to be almost the same.

The lowest magnetic configuration of $La^{3+}Ti^{4+}Mn^{3+}Ni^{2+}O_6$ is found to be A-type AFM ordering as described in Fig. 4(c), followed by the FM configuration. The corresponding electronic structure is shown in Fig. 4(d). The AFM ordering with the absence of an inversion center indicates that this compound is important for multifunctional properties. Other collinear spin configurations as shown in Fig. 5, are found to be stable within an enhanced energy window ($\sim$20 meV), as shown in Table V, in contrast to those in Ref. [19] with reference to A-type AFM ordering. This indicates that we may achieve strong magnetic exchange interactions for $LaTiMnNiO_6$ compared to $CaMnTi_2O_6$.

The magnetic polar behavior of LFMNO and LTMNO makes them superior compounds in the family. Furthermore, we identify LFMNO and LTMNO as direct band gap semiconductors with energy gaps of 1.40 and 1.18 eV, respectively, as presented in Fig. 6. This may make visible light absorption easier for them. Density of states (DOS) analysis of LFMNO
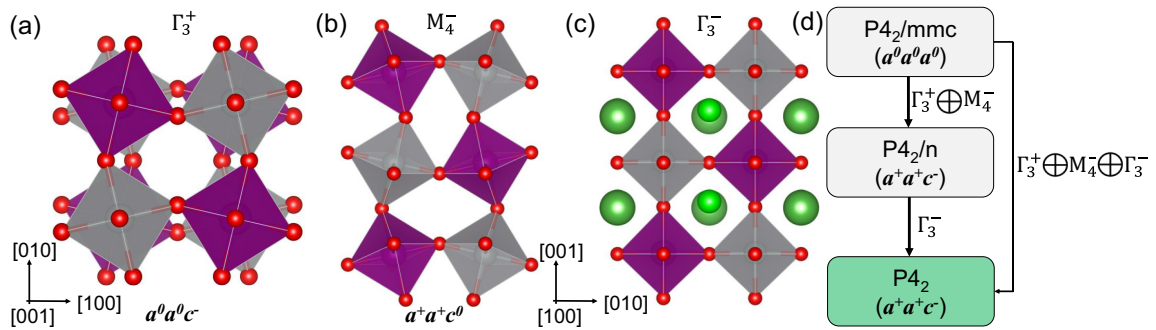

FIG. 2. The low-symmetry ferroelectric $P4_2$ phase of LaMMnNiO$_6$ compounds for $a^+a^+c^-$ rotation is related to the centrosymmetric $P4_2/mmc$ reference structure through three major structural distortions: (a) out-of-phase ($a^0a^0c^-$) rotation of Fe/TiO$_6$ octahedra along the c axis, denoted by the Γ_3^+ irreducible representation (irrep), (b) in-phase ($a^+a^+c^0$) rotation of Fe/TiO$_6$ octahedra along the crystallographic a and b axes, represented by the M$_4^-$ irrep, and (c) ferroelectric displacement of the Fe/Ti cations from the square plane of Fe/TiO$_4$ described by Γ_3^-. (d) The group-subgroup tree for our systems; the ferroelectric $P4_2$ phase is highlighted in green. The La and Fe/Ti atoms are omitted from the first two structures for clarity.
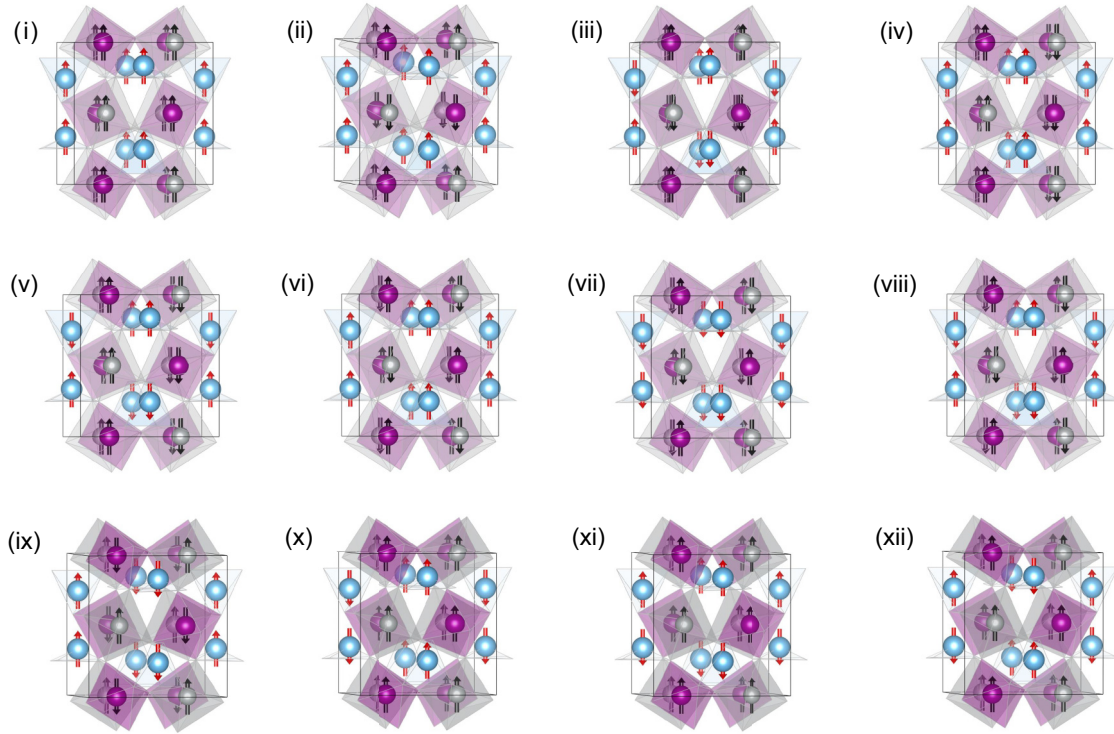
FIG. 3. Various spin configurations of LaFeMnNiO$_6$ within the collinear picture. The nonmagnetic atoms are not shown for better clarity. The Fe, Mn, and Ni atoms are denoted by blue, magenta, and silver balls, respectively.

reveals that a local moment of $4.21\mu_B$/Fe with filled d orbitals in the up spin channel (USC) suggests a nominal charge state of Fe^{3+} ($t_{2g}^3 e_g^2$) is in a high-spin state and is shown in Fig. 4(b). The octahedral environment of the Mn and Ni atoms shows
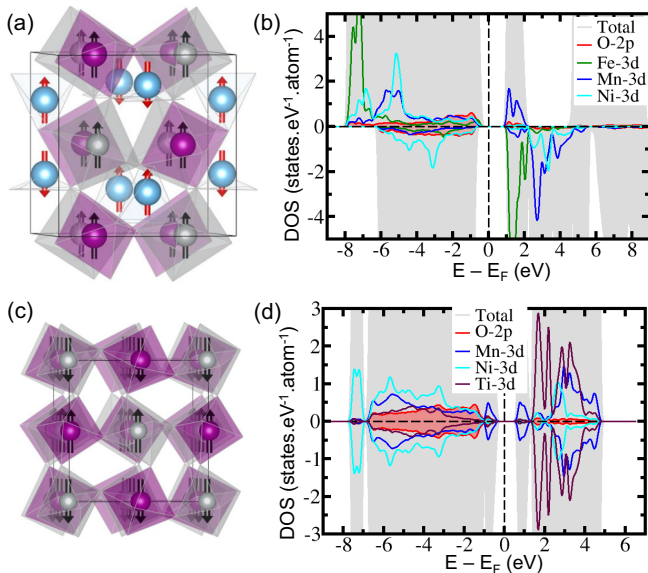

FIG. 4. Ground state spin configurations and corresponding electronic structures of LaFeMnNiO$_6$ (top panel) and LaTiMnNiO$_6$ (bottom panel). The nonmagnetic atoms are not shown for clarity. The Fe, Mn, and Ni atoms are described by blue, magenta, and silver balls, respectively.

t_{2g} and e_g crystal field splitting. Ni t_{2g} and Ni e_g bands in the USC lie between -8 eV energy and the Fermi energy E_F and show strong hybridization with Mn d and O p. However, Ni t_{2g} bands in the down spin channel (DSC) are localized between O p and the Fermi level. The e_g levels in the DSC are located above E_F. This DOS along a local moment of $1.71\mu_B$/Ni indicates a nominal charge state of Ni^{2+} ($t_{2g}^6 e_g^2$). The filled Mn t_{2g} bands are located between the Ni t_{2g} and Ni e_g levels in the USC. Mn t_{2g} in the DSC is totally empty, while Mn e_g in both spin channels are found above the Fermi level and an insulting phase is obtained analogous to that in Ref. [41]. This suggests a nominal charge state of Mn^{4+} ($t_{2g}^3 e_g^0$) with a local moment of $3.16\mu_B$/Mn.

Investigating the partial DOS of LTMNO shows us Ti d states are mostly empty, suggesting a d^0 configuration (Ti^{4+}), as shown in Fig. 4(d). Due to the octahedral environment in MnO$_6$, and NiO$_6$ the d orbitals split into t_{2g} and e_g levels, similar to LFMNO. As discussed earlier, the Mn-Ni interaction in LTMNO between layers (A-type AFM ordering) is antiferromagnetic, and hence, the DOS is identical in the two spin channels. However, if we consider any FM pair of Mn and Ni atoms, we find a similar electronic structure for Ni^{2+} ($t_{2g}^6 e_g^2$), as shown in Fig. 7. To understand the nominal charge state of Mn sublattices, we consider any ferromagnetic pair between Mn and Ni (say, the bottom layer). Filled Mn t_{2g} bands (below the Fermi level E_F) are found between -8 and -0.5 eV in the up spin channel as shown in Fig. 7. There is no contribution from Mn t_{2g} in the down spin channel below E_F. This suggests the Mn t_{2g}^3 electronic structure. We can see the Mn e_g contribution both below and above E_F in the up spin channel, while there is no contribution below E_F in the down
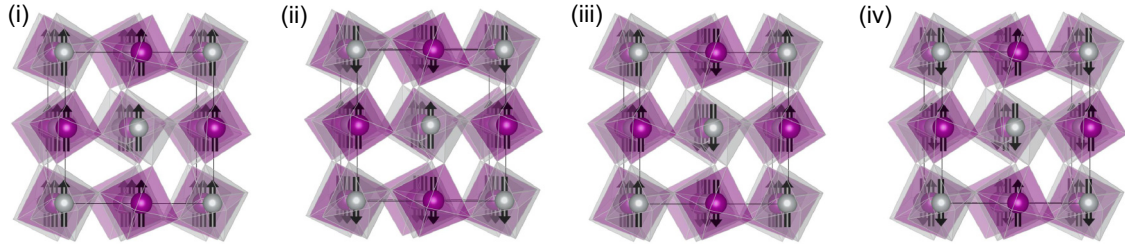
FIG. 5. Various spin configurations of LaTiMnNiO$_6$ within the collinear picture. The nonmagnetic atoms are not shown for better clarity. The Mn and Ni atoms are denoted by magenta and silver balls respectively.

spin channel. This again suggests a Mn e_g^1 state. Therefore, the electronic configuration for manganese is Mn $t_{2g}^3 e_g^1$. The local moment of 3.82μ_B/Mn again shows that there are four unpaired electrons. This in turn implies the nominal charge state 3+ for the Mn atom.

C. Monte Carlo simulations

The calculated intersite exchange parameters for both compounds are shown in Fig. 8. The first observation is that the magnetic couplings decrease rapidly as the M-M distance increases; only the contributions from the first few nearest neighbors play an important role in determining the magnetic ground state. This result provides direct evidence that the character of the d electrons in transition metal elements is predominantly localized, thereby demonstrating the rationality and effectiveness of the Heisenberg model used in this study.

For LaFeMnNiO$_6$, the interactions among the different transition metal elements—Fe, Mn, and Ni—vary in nature: the Mn-Ni coupling is ferromagnetic, whereas the Fe-Mn and Fe-Ni couplings contribute to antiferromagnetic interaction. Furthermore, different from the nearest Ni-Ni and Mn-Mn pairs with a relatively large distance (nearly a unit cell), the two Fe-Fe pair distances are relatively small and therefore exhibit noticeable antiferromagnetic coupling. These observations align perfectly with the ferrimagnetic ground state configuration obtained from our total energy calculations. With an average Ni-Mn ferromagnetic coupling of 0.33 mRy and Fe-Mn and Fe-Ni antiferromagnetic couplings of −0.35 and −0.28 mRy, respectively, in addition to strong and weak antiferromagnetic Fe-Fe couplings of −0.42 and −0.06 mRy, the system exhibits a remarkable magnetic transition temperature of 225 K, as shown in the inset of Fig. 8(a). In contrast, couplings in LaTiMnNiO$_6$ are relatively simple. The only two transition metal elements, Mn and Ni, form a specific AFM configuration, with contributions from both AFM and FM

interactions coming from the first nearest neighbors. Owing to the smaller number of magnetic elements and weaker exchange parameters in this compound, the magnetic transition temperature is predicted to be 48 K. This is illustrated in the inset of Fig. 8(b).

D. Computation of formation energies

To identify the correct reaction sequence, we follow a theoretical framework suggested by Akbarzadeh *et al.* [42] and make appropriate modifications to suit our problems [14,43]. The reaction energy is calculated by the following expression:

$$G = \sum_i x_i F_i, \tag{2}$$

where G is the total reaction energy of the reaction sequences, i includes a set of all possible stable oxides, F is the free energy (at $T = 0$ K) of the ith compound, and x_i (unknown) is the variable molar fraction of the ith compound at a given composition. To get the minimum energy reaction, we minimize Eq. (2) with respect to the molar fraction x_i, with mass conservation constraints such as

$$f_s = \sum_i x_i n_i^s = \text{const}, \tag{3}$$

where n_i^s is the number of ions of species s in the ith compound per formula unit and f_s is the molar fraction of the individual species s (s = La, Ti, Fe, Mn, Ni, and O). To apply the above formalism, we consider a set of all possible stable compounds from the Materials Project database [44] that contains La, Ti, Fe, Mn, Ni, and O as the constituents of the DDPOs and are listed in Table VI. We calculate the free energy of these compounds using the same parameters that we used to calculate the energies of DDPOs. Using these calculated free energies, we minimize the linear Eq. (2) using a linear programming solver and calculate the formation energies with respect to these minimum energy reactions. The thermodynamic stability is one of the requirements to

TABLE V. Relative energies for all possible collinear spins with reference to the magnetic ground state of LaTiMnNiO$_6$.

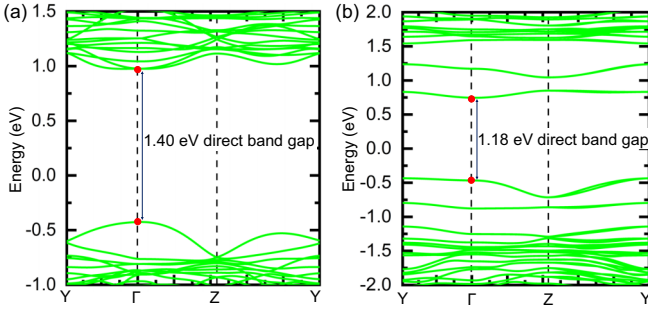|	Collinear spin configuration		
	A-type AFM [Fig. 5, panel (ii)]	C-type AFM [Fig. 5, panel (iii)]	G-type AFM [Fig. 5, panel (iv)]	FM [Fig. 5, panel (i)]
Energy (meV)	0.0	17.1	9.4	16.2

FIG. 6. Calculated electronic band structure from GGA+U calculations for (a) LaFeMnNiO$_6$ and (b) LaTiMnNiO$_6$ DDPOs.

realize the practical applications of a compound. We therefore examine the formation energies of the LFMNO and LTMNO DDPOs. We calculate the formation energies of these systems by considering the decomposition reaction of DDPOs via the most probable reaction pathways by utilizing a linear programming problem combined with the grand canonical method [14]. The detailed methodology is provided in the method section. We consider the stable oxides that were reported in the Inorganic Crystal Structure Database [45] and in the Materials Project [44] in our study. The minimum energy decomposition paths for these compounds are

$$
\begin{aligned}
\Delta_f E_1 &= [\text{LaFeMnNiO}_6] \\
&= E[\text{LaFeMnNiO}_6] \\
&\quad - \left(\tfrac{3}{6} E[\text{La}_2\text{O}_3] + \tfrac{3}{6} E[\text{Fe}_2\text{O}_3] + \tfrac{1}{6} E[\text{Mn}_3\text{O}_4] \right. \\
&\quad \left. + \tfrac{3}{6} E[\text{MnO}_2] + \tfrac{2}{6} E[\text{Ni}_3\text{O}_4] \right), \quad (4)
\end{aligned}
$$

$$
\begin{aligned}
\Delta_f E_2 &= [\text{LaTiMnNiO}_6] \\
&= E[\text{LaTiMnNiO}_6] \\
&\quad - \left(\tfrac{3}{6} E[\text{La}_2\text{Ti}_2\text{O}_7] + \tfrac{2}{6} E[\text{Mn}_3\text{O}_4] + \tfrac{3}{6} E[\text{NiO}] \right. \\
&\quad \left. + \tfrac{1}{6} E[\text{Ni}_3\text{O}_4] \right). \quad (5)
\end{aligned}
$$

With the implementation of these equations, the formation energies of LFMNO and LTMNO are found to be 1.25 and 0.89 eV, respectively. These values are in agreement with the experimental observations as the DDPOs are synthesized
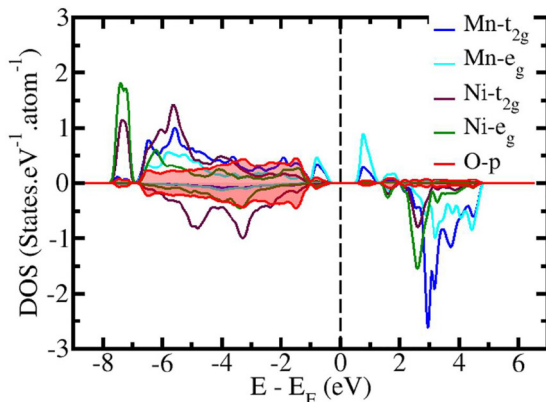

FIG. 7. Orbital-resolved electronic structure from the GGA+U calculation for LaTiMnNiO$_6$ DDPO.

TABLE VI. List of stable oxides considered for computing the formation energies of the double-double perovskites.

Stable oxide	Space group	Stable oxide	Space group
La$_2$O$_3$	Ia-3	TiNiO$_3$	R-3
La$_2$TiO$_5$	$Pnma$	TiMnO$_3$	R-3
La$_2$Ti$_2$O$_5$	$P2_1$	TiMn$_2$O$_4$	$P4_32_2$
Ti$_2$O	P-3m_1	Mn$_2$O$_3$	$Pbca$
Ti$_2$O$_3$	R-3c	MnO$_2$	$I4/m$
Ti$_3$O$_5$	$C2/m$	MnO	Fm-3m
Ti$_6$O	P-31c	LaNiO$_3$	R-3c
TiO	P-62m	MnNiO$_3$	R-3
NiO	Fm-3m	Fe$_2$NiO$_4$	$Imma$
Ni$_3$O$_4$	$Cmmm$	Mn$_3$O$_4$	$I41/amd$
LaFeO$_3$	R-3c	FeO	$C2/m$
FeO	$C2/m$	Fe$_2$O$_3$	R-3c
Ti$_3$O	P-31c	TiO$_2$	$C2/m$

under high pressure (∼10–15 GPa) and high temperature (∼1200–1700 °C) [21,40].

IV. CONCLUSION

In summary, our investigation based on DFT calculations and symmetry analysis revealed the presence of direct gap semiconductors, with GGA+U forbidden energy values of 1.40 and 1.18 eV for LFMNO and LTMNO, respectively, suggesting potential suitability for visible light absorption. We elucidated the origins of these magnetic polar semiconductors. The observed long-range ferrimagnetic ordering in LFMNO is attributed to superexchange interactions. Through Monte Carlo simulations, we determine magnetic transition temperatures of 225 and 48 K for LFMNO and LTMNO, respectively, which are significantly higher than the approximately 10 K observed in CaMnTi$_2$O$_6$. The calculated spontaneous polarization values are found to be 20.0 and 21.8μC/cm^2 for LFMNO and LTMNO respectively. Our measurements of the values of spontaneous polarization are encouraging in the context of designing multiferroic materials with strong magnetoelectric coupling. Determining the spontaneous polarization of a ferroelectric material typically involves experimental techniques that specifically designed to measure electric polarization [46–52]. We believe the mentioned experimental methods could also be used to determine the spontaneous polarizations for LFMNO and LTMNO and can be compared with the computed values. In conclusion, both LFMNO and LTMNO emerge as promising multiferroics, featuring magnetic transition metals in the B and B' sublattices in addition to a TM at the A' site.
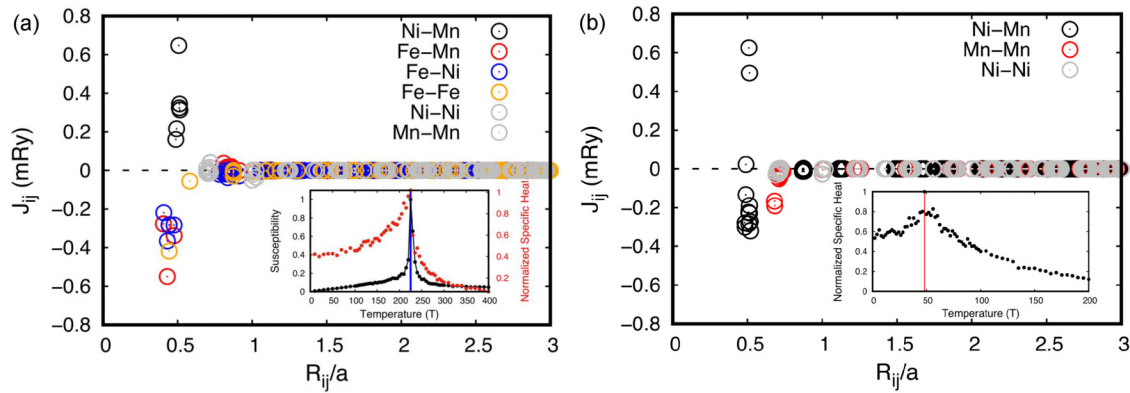
FIG. 8. Calculated intersite exchange parameters for each *M-M* pair as a function distance for $LaFeMnNiO_6$ and $LaTiMnNiO_6$. The positive and negative values represent ferromagnetic and antiferromagnetic couplings, respectively. The inset shows the normalized specific heat (black circles) and the magnetization (red circles) as a function of temperature, calculated from classical Monte Carlo simulations. The blue vertical line indicates the magnetization transition temperature.

[1] Y. Tokura, S. Seki, and N. Nagaosa, Rep. Prog. Phys. **77**, 076501 (2014).

[2] F. Matsukura, Y. Tokura, and H. Ohno, Nat. Nanotechnol. **10**, 209 (2015).

[3] J. A. Mundy *et al.*, Nature (London) **537**, 523 (2016).

[4] M. Fiebig, T. Lottermoser, D. Meier, and M. Trassin, Nat. Rev. Mater. **1**, 16046 (2016).

[5] N. A. Spaldin and R. Ramesh, Nat. Mater. **18**, 203 (2019).

[6] A. A. Belik, Dalton Trans. **47**, 3209 (2018).

[7] S. Ghosh, H. Das, and C. J. Fennie, Phys. Rev. B **92**, 184112 (2015).

[8] M. Shaikh, M. Karmakar, and S. Ghosh, Phys. Rev. B **101**, 054101 (2020).

[9] N. A. Spaldin and M. Fiebig, Science **309**, 391 (2005).

[10] W. Eerenstein, N. Mathur, and J. F. Scott, Nature (London) **442**, 759 (2006).

[11] R. Ramesh and N. A. Spaldin, Nat. Mater. **6**, 21 (2007).

[12] W. Känzig, Solid State Phys. **4**, 1 (1957).

[13] W. Cochran, Phys. Rev. Lett. **3**, 412 (1959).

[14] M. Shaikh, A. Fathima, M. Swamynadhan, H. Das, and S. Ghosh, Chem. Mater. **33**, 1594 (2021).

[15] A. Ghosh, G. Palanichamy, D. P. Trujillo, M. Shaikh, and S. Ghosh, Chem. Mater. **34**, 7563 (2022).

[16] P. Gayathri, S. Ghosh, and A. Ghosh, Chem. Mater. **36**, 682 (2024).

[17] A. Aimi, D. Mori, K.-I. Hiraki, T. Takahashi, Y. J. Shan, Y. Shirako, J. Zhou, and Y. Inaguma, Chem. Mater. **26**, 2601 (2014).

[18] E. Solana-Madruga, Á. M. Arévalo-López, A. J. Dos Santos-García, E. Urones-Garrote, D. Ávila-Brande, R. Sáez-Puche, and J. P. Attfield, Angew. Chem., Int. Ed. **55**, 9340 (2016).

[19] G. Gou, N. Charles, J. Shi, and J. M. Rondinelli, Inorg. Chem. **56**, 11854 (2017).

[20] Z. Li *et al.*, J. Am. Chem. Soc. **140**, 2214 (2018).

[21] K. Ji, J. Bedward, Q. Li, P. Manuel, C. Ritter, and J. P. Attfield, Chem. Commun. **59**, 6371 (2023).

[22] K. Leinenweber and J. Parise, J. Solid State Chem. **114**, 277 (1995).

[23] C. J. Howard and H. T. Stokes, Acta Crystallogr. Sect. B **54**, 782 (1998).

[24] X. Li, W. M. Xu, M. A. McGuire, Y. Cho, M. C. Downer, Y. Wan, X. Y. Li, Z. Y. Li, Q. Cui, J.-G. Cheng, J. B. Goodenough, and J. S. Zhou, Phys. Rev. B **98**, 064201 (2018).

[25] A. M. Glazer, Acta Crystallogr. Sect. B **28**, 3384 (1972).

[26] P. Hohenberg and W. Kohn, Phys. Rev. **136**, B864 (1964).

[27] R. D. King-Smith and D. Vanderbilt, Phys. Rev. B **47**, 1651 (1993).

[28] G. Kresse and J. Furthmüller, Phys. Rev. B **54**, 11169 (1996).

[29] S. L. Dudarev, G. A. Botton, S. Y. Savrasov, C. J. Humphreys, and A. P. Sutton, Phys. Rev. B **57**, 1505 (1998).

[30] J. P. Perdew, A. Ruzsinszky, G. I. Csonka, O. A. Vydrov, G. E. Scuseria, L. A. Constantin, X. Zhou, and K. Burke, Phys. Rev. Lett. **100**, 136406 (2008).

[31] K. Momma and F. Izumi, J. Appl. Crystallogr. **41**, 653 (2008).

[32] K. Kunc and R. M. Martin, Phys. Rev. Lett. **48**, 406 (1982).

[33] H. T. Stokes, D. M. Hatch, B. J. Campbell, and D. E. Tanner, J. Appl. Crystallogr. **39**, 607 (2006).

[34] A. Liechtenstein, M. Katsnelson, V. Antropov, and V. Gubanov, J. Magn. Magn. Mater. **67**, 65 (1987).

[35] J. M. Wills, M. Alouani, P. Andersson, A. Delin, O. Eriksson, and O. Grechnyev, *Full-Potential Electronic Structure Method: Energy and Force Calculations with Density Functional and Dynamical Mean Field Theory* (Springer, Berlin, 2010), Vol. 167.

[36] O. Eriksson, A. Bergman, L. Bergqvist, and J. Hellsvik, *Atomistic Spin Dynamics: Foundations and Applications* (Oxford University Press, Oxford, 2017).

[37] Y. Zhang, J. Sun, J. P. Perdew, and X. Wu, Phys. Rev. B **96**, 035143 (2017).

[38] H. T. Stokes, D. M. Hatch, and J. D. Wells, Phys. Rev. B **43**, 11010 (1991).

[39] See Supplemental Material at http://link.aps.org/supplemental/10.1103/PhysRevB.109.174115 for the mode amplitudes of in-phase rotation and out-of-phase rotation and the relative energies obtained through ionic iterations. The relative energies are computed with reference to the high-symmetry structure.

[40] G. M. McNally, Á. M. Arévalo-López, P. Kearins, F. Orlandi, P. Manuel, and J. P. Attfield, Chem. Mater. **29**, 8870 (2017).

[41] H. Das, U. V. Waghmare, T. Saha-Dasgupta, and D. D. Sarma, Phys. Rev. Lett. **100**, 186402 (2008).

[42] A. R. Akbarzadeh, V. Ozoliņš, and C. Wolverton, Adv. Mater. **19**, 3233 (2007).

[43] D. Wang, M. Shaikh, S. Ghosh, and B. Sanyal, Phys. Rev. Mater. **5**, 054405 (2021).

[44] A. Jain *et al.*, APL Mater. **1**, 011002 (2013).

[45] A. Belsky, M. Hellenbrandt, V. L. Karen, and P. Luksch, Acta Crystallogr. Sect. B **58**, 364 (2002).

[46] M. Ayoub, H. Futterlieb, J. Imbrock, and C. Denz, Adv. Mater. **29**, 1603325 (2017).

[47] F. Rubio-Marcos, D. A. Ochoa, A. Del Campo, M. A. García, G. R. Castro, J. F. Fernández, and J. E. García, Nat. Photonics **12**, 29 (2018).

[48] B. Knabe, K. Buse, W. Assenmacher, and W. Mader, Phys. Rev. B **86**, 195428 (2012).

[49] T.-T. Ying, H.-J. Shi, S.-P. Chen, Y.-Z. Tang, Y.-H. Tan, S.-F. Wang, Z. Sun, F. X. Wang, and M.-Y. Wan, Inorg. Chem. **62**, 6189 (2023).

[50] N. Leblanc, N. Mercier, L. Zorina, S. Simonov, P. Auban-Senzier, and C. Pasquier, J. Am. Chem. Soc. **133**, 14924 (2011).

[51] Z. Sun, X. Yi, K. Tao, C. Ji, X. Liu, L. Li, S. Han, A. Zheng, M. Hong, and J. Luo, Angew. Chem., Int. Ed. **57**, 9833 (2018).

[52] R. Takahashi, H. Misumi, and M. Lippmaa, Phys. Rev. B **86**, 144105 (2012).